

See discussions, stats, and author profiles for this publication at: <https://www.researchgate.net/publication/263940918>

Controlling Nanoparticle Dynamics in Conical Nanopores

ARTICLE *in* THE JOURNAL OF PHYSICAL CHEMISTRY C · DECEMBER 2012

Impact Factor: 4.77 · DOI: 10.1021/jp310513v

CITATIONS

22

READS

43

4 AUTHORS, INCLUDING:



Sean R German

University of Utah

7 PUBLICATIONS 45 CITATIONS

SEE PROFILE



Long Luo

University of Texas at Austin

13 PUBLICATIONS 72 CITATIONS

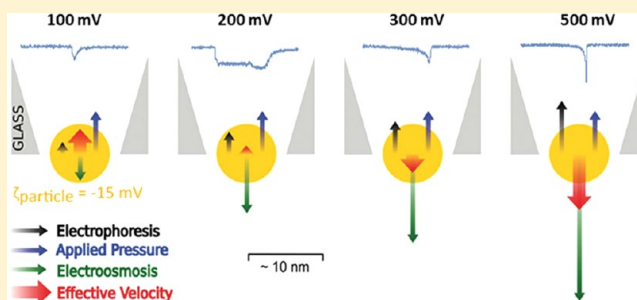
SEE PROFILE

Controlling Nanoparticle Dynamics in Conical Nanopores

Sean R. German,[†] Long Luo,[‡] Henry S. White,[‡] and Tony L. Mega^{*,†}[†]Revalerio Corporation, 1200 East D Street, Tacoma, Washington 98421, United States[‡]Department of Chemistry, University of Utah, 315 S 1400 E, Salt Lake City, Utah 84112, United States

S Supporting Information

ABSTRACT: Conical nanopores are a powerful tool for characterizing nanoscale particles and even small molecules. Although the technique provides a wealth of information, such pores are limited in their ability to investigate particle dynamics due to high particle velocities through a very short sensing zone. In this report, we demonstrate the use of applied pressure to balance electrokinetic forces acting on 8 nm diameter Au nanoparticles as they translocate through a ~10 nm diameter orifice. This force balance provides a means to vary nanoparticle velocity by 3 orders of magnitude, allowing for their detection and characterization on time scales as long as 100 ms. We studied nanoparticles having different zeta potentials by varying salt concentration, applied pressure, and voltage to reveal the point at which forces are balanced and the particle velocities approach zero. Variation of the voltage around this force balance point provides a means to precisely control the magnitude and direction of the particle translocation velocity. Nanoparticle velocities computed from finite-element simulations as a function of applied pressure and voltage yield predictions in semiquantitative agreement with the experimental results. Optimizing the conditions of these techniques will allow the characterization of particles and their dynamics down to the smallest end of the nanoscale range.



Characterization of the geometry, charge, and dynamic properties of individual nanoscale objects in bulk solution presents a significant challenge, particularly for objects at the lower end of the scale. Transmission electron microscopy (TEM) does not assess particles in bulk solution, and dynamic light scattering (DLS) does not provide information about individual particles. Furthermore, these techniques are prone to artifacts.¹ By contrast, resistive pulse analyses using nanopores provide a method that measures individual nanoscale particles in bulk solution as well as providing information about particle charge. Recent adaptations of the Coulter-counter technique to the nanoscale range have been used as a label-free method for studying biological molecules, especially DNA, and nanoparticles having a variety of compositions and surface charges.² In these techniques, an electrical potential difference is applied between the electrodes on the two sides of a nanopore. Nanoparticles passing through the pore cause a brief decrease in the electrical current plotted as a function of time. The duration, magnitude, and shape of these current–time profiles provide a wealth of information about the forces that act on the nanoparticles as they pass through the pore.^{2,3} However, large particle velocities can limit the application of this technique to a significant portion of the nanoscale range.

Reliable detection and characterization of small nanoparticles are limited by electronic filtering, which for typical bandwidths of 10 kHz leads to an underestimation of peak heights for detectable particles and can even entirely miss particles below 40 nm for certain pore geometries.³ Innovative attempts to overcome the problem of excessive translocation speed include

chemical modification of pores⁴ and variations in pore size,⁵ pore shape,⁶ salt concentration, temperature, and solution viscosity,⁷ as well as employing repeated measurements of individual particles.^{8,9} By varying pH to adjust the difference in zeta potential between the particle and the pore, Firnkes et al. were able to manipulate the effective velocity of a single protein and to reverse the translocation driving force from electrophoretic to electroosmotic.¹⁰ While this method provides an important step forward in controlling particle speed, significant diffusion rates across the 10 nm wide pore reduce signal fidelity.

Cylindrical carbon nanotubes¹¹ and glass nanochannels¹² have been used to characterize 60 and 40 nm particles, respectively, but measurement of smaller particles was hindered by low signal-to-noise ratios. By contrast, focusing of the sensing zone in conical nanopores to a much smaller volume imparts many advantages including high signal-to-noise ratios and asymmetric peak shapes, which provide information about translocation direction.³ Recently, Vogel et al. reported a method for characterizing the surface charge of 200 nm particles based upon resistive pulse sensing in conical nanopores under variable pressure.¹³ The elastomeric pores used in these studies have the advantage that they can be dynamically varied in size; however, the hydrophobic nature of this pore material may lead to undesirable interactions with hydrophobic analytes and solvents other than water. By

Received: October 23, 2012

Revised: November 29, 2012

Published: December 3, 2012



contrast, the hydrophilic surfaces of silicon nitride (SiN) and glass nanopores (GNPs) are often desirable for studies involving both hydrophobic and hydrophilic analytes. SiN pores are frequently used to study nucleic acids and other large aspect ratio particles,¹⁴ but there are far fewer studies of low aspect ratio (spherical) particles below 40 nm,¹⁵ likely due to excessive particle speeds through a short sensing zone. SiN pores have the advantage that pore size is readily measured during their production, but the process is not simple and quite expensive.

By contrast, simple and inexpensive methods exist for producing GNPs that can detect low aspect ratio molecules as small as 1.5 nm.^{16,17} In addition to hydrophilicity, GNPs have numerous advantages compared to other types of pores in terms of exceptional electrical properties for high bandwidth measurements, ability to withstand high pressure, compatibility with optical measurements, chemical stability, and the possibility to modify their surface with a variety of functional groups. Gao et al. reduced particle velocities sufficiently to detect 10 nm gold nanoparticles by producing GNPs near the threshold at which the particle could pass through.¹⁶ Though inadequate for general control of particle dynamics, this approach did provide a method for determining pore size, which was not possible using electron microscopy.^{16,17} In this paper, we further characterize the threshold condition, and demonstrate control of velocities over 3 orders of magnitude for 8 nm nanoparticles in GNPs. Finite element analysis (FEA) simulations are used to verify these experimental results providing further insights into pore geometry, spatial distribution of particle velocities within the pore, and the influence of both the particle and pore surface charge densities. We provide a rationale for how particle dynamics are controlled by balancing the pressure, electrophoretic (EPF), and electroosmotic (EOF) forces (Figure 1). This balance of three forces provides previously unattainable control over particle dynamics in a conical pore.

RESULTS AND DISCUSSION

Detecting Nanoparticles at the Threshold of the Pore Size. Micropipet GNPs were prepared by a modification of the method described by Gao et al.¹⁶ (Figure 2). Determining the size of a micropipet GNP is not simple, and others have reported being unable to obtain SEM images of the pore.^{16,17} Here we report SEM images of a micropipet GNP used to measure 8 nm diameter gold nanoparticles (Figure 3). Although the diameter of the pore was found to be 37 nm at the surface, the pore may narrow just below the surface due to the etching procedure. On the basis of the microscopy images (Figure 2A,B) and the characteristic asymmetric translocation profiles and FEA simulations, *vide infra*, we believe that the inner pore geometry is conical with a $\sim 2^\circ$ half-cone angle.¹⁸ A subsequent report concerning the inner pore geometry is in preparation.

Identifying the size of a particle at the threshold of passing through the pore provides an alternative to SEM imaging for sizing micropipet-based GNPs. We performed experiments to detect nanoparticle translocations using 8 nm diameter carboxy methyl polymer-coated Au nanoparticles having small standard deviation in size (± 0.6 nm), and at a typical concentration of 200 nM in a 1.0 M NaCl solution. Current versus time ($i-t$) traces were recorded while a positive potential was applied to an Ag/AgCl wire electrode within the micropipet relative to the external solution. We first produced the smallest pores possible

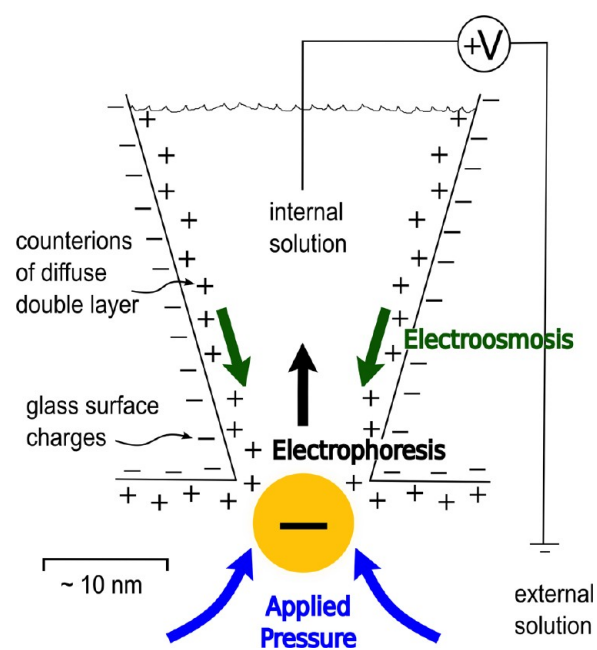


Figure 1. Driving forces acting on a particle in a conical nanopore. During translocation experiments, positive potentials applied to an electrode within the pipet and negative pressures applied within the pipet both tend to draw negatively charged particles inward from the external solution. The applied potential also induces a counteracting electroosmotic force that tends to drive particles out of the pipet into the external solution. The summation of these different forces determines the particle velocity and translocation time scale.

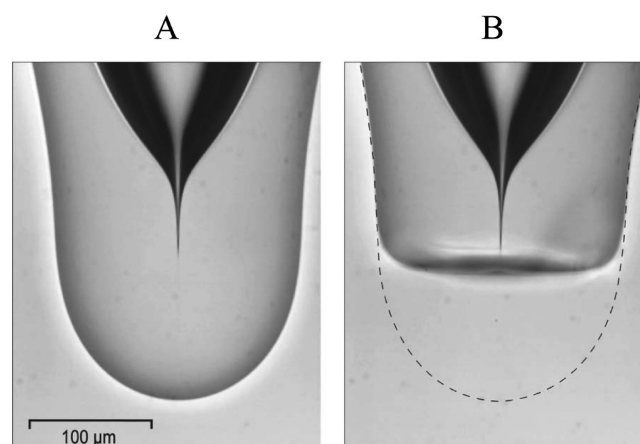


Figure 2. (A) A programmable micropipet puller was used to form a narrow opening (1 μm) that was melted into a terminal bulb enclosing a cone-shaped cavity. (B) The terminal bulb was then sanded and briefly melted with a microforge to form a flattened geometry (dashed lines delineate the outlines of the original bulb shown in (A)). Ag/AgCl electrodes were placed across the unopened pore and hydrofluoric acid etchant was used as the external solution to form a nanoscale pore in the sanded and remelted tip. A spike in the current indicated pore formation.

(having a resistance between 100 and 200 M Ω , measured in 1.0 M NaCl), and repeatedly widened them with dilute etchant until we detected pressure-driven nanoparticle translocations. This approach enabled us to detect cases in which square blocks were terminated with a sharp resistive pulse as illustrated by the 17 pA current block in Figure 4B, which ends with a 70 pA peak before returning to the base current. Since this

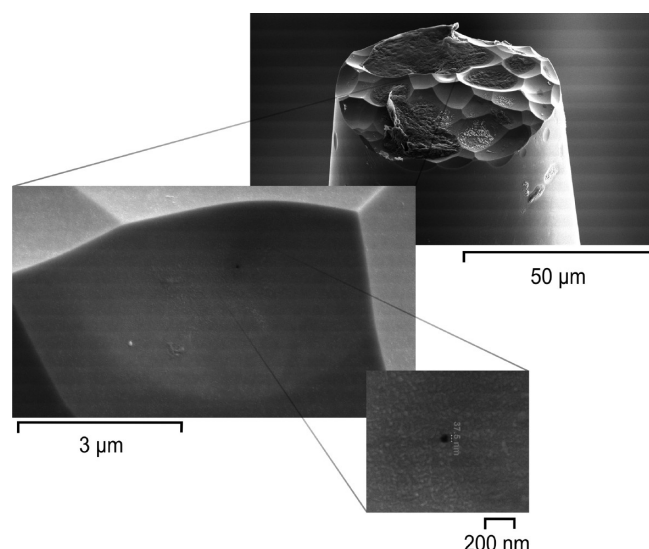


Figure 3. Scanning electron microscope (SEM) images of a nanopore in a micropipet tip that had been used to detect 8 nm nanoparticles. Prior to imaging, this nanopore was rinsed with deionized water, allowed to dry, and then sputtered with a ~ 2 nm thick layer of gold. The opening located at the center of the pipet tip has a diameter of 37 nm at the surface.

terminal spike is large and has the asymmetric triangular shape typical of a particle translocation through a conical pore, we believe it represents a particle passing through the pore after an initial partial blockade of the opening. Vercoutere et al. observed similar long shallow blockades caused by individual hairpin DNA molecules prior to a rapid deep blockade indicating translocation of the DNA through an α -hemolysin pore.¹⁹ Though the geometrical considerations for gold nanoparticles are much simpler, it is possible that the particle coating requires time to compress in order for the particle to fit

through the pore at the threshold size. Gao et al. also used the threshold condition to estimate the size of their pores using DNA, 10 nm Au nanoparticles, and even single molecules of β -cyclodextrin, based on simple square-shaped blocks lacking a terminal spike.¹⁶ On the basis of repeated observations of this kind, we conclude that the occurrence of square blockages without a sharp spike at the end (Figure 4A) represents transient blockages of the nanopore orifice by the Au nanoparticles without translocation through the pore.

Particle Capture and Release. Applying pressure within the pipet offers considerable control over particle translocation, including the ability to draw individual particles into the pore and to push them out again repeatedly, as illustrated in Figure S1 in the Supporting Information. Because the quasi-triangular peak shape depends on the direction of translocation, these experiments provide confirmation that our pores are conically shaped and open inwardly. Similar observations of particle reversal with application of pressure have been used to measure the size of individual particles depending upon their recapture probability.²⁰ The distinct differences seen in translocation shape for individual particles in Figure S1 reflect the acute sensitivity of this technique to monitor subtle nanopore/nanoparticle characteristics that are most likely based on geometrical and charge interactions.

Figure 5 demonstrates that varying the applied potential can also be used to drive particles into and out of a pore repeatedly. In the experimental results shown in Figure 5A,B, no pressure was applied to the pipet, but instead the particle motion followed a 10 Hz square wave varying between +1.0 and -1.0 V. The four occasions of a particle going into and out of the pore were preceded and followed by several seconds without any particle translocations, suggesting that we observed the repeated translocations of a single particle. Similar voltage switching experiments have been used to recapture individual DNA strands.⁹ Reversing voltage polarity is not required for

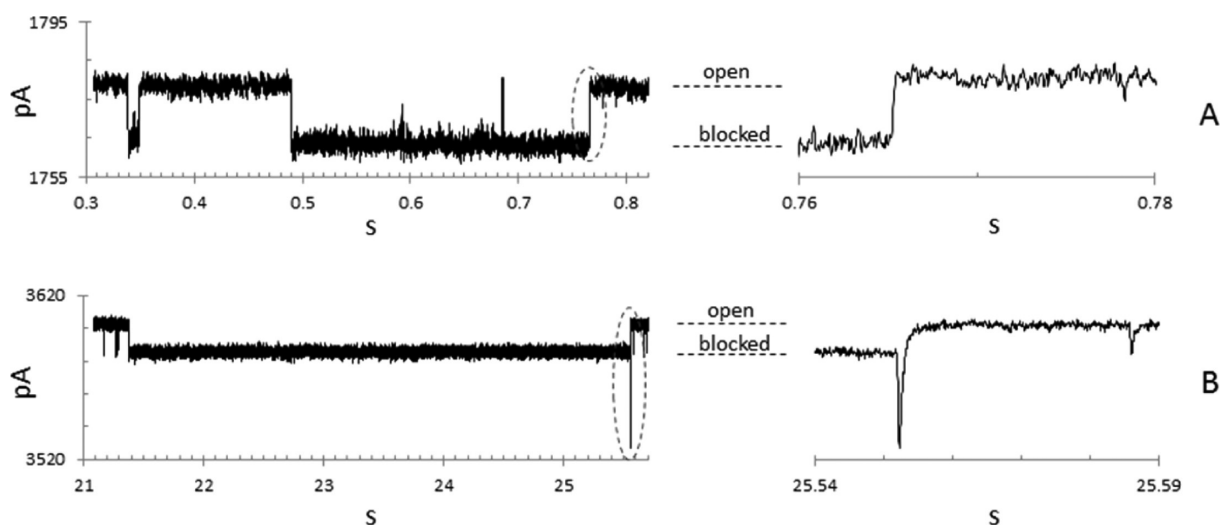


Figure 4. i - t traces used to determine when the pore size exceeds or is just at the threshold of the Au nanoparticle size. In these experiments, 8 nm Au nanoparticles ($\zeta = -51$ mV) were placed in the external solution, and a pressure of ~ 0.5 atm and voltage of 250 mV were applied to drive the particles into the nanopore. (A) Square-shaped blockades of widely varying duration are observed when the pore size is smaller than the particle size. The current within these blocks sometimes increases briefly, as seen at 0.59 and 0.68 s, but eventually returns to the base current level as seen in the dashed oval in (A) (the trace on the right is an expansion of this region). (B) Passage of a particle through another pore at the threshold of the particle size accompanied by a large current spike (dashed oval in (B)). Note that this current spike (expanded on the right) has the asymmetric shape characteristic of a typical translocation through a conical pore. The 1.0 M NaCl solution was buffered at pH 7.4 with 7 mM Na_2HPO_4 , 21 mM KH_2PO_4 , and contained 0.1% Triton X-100.

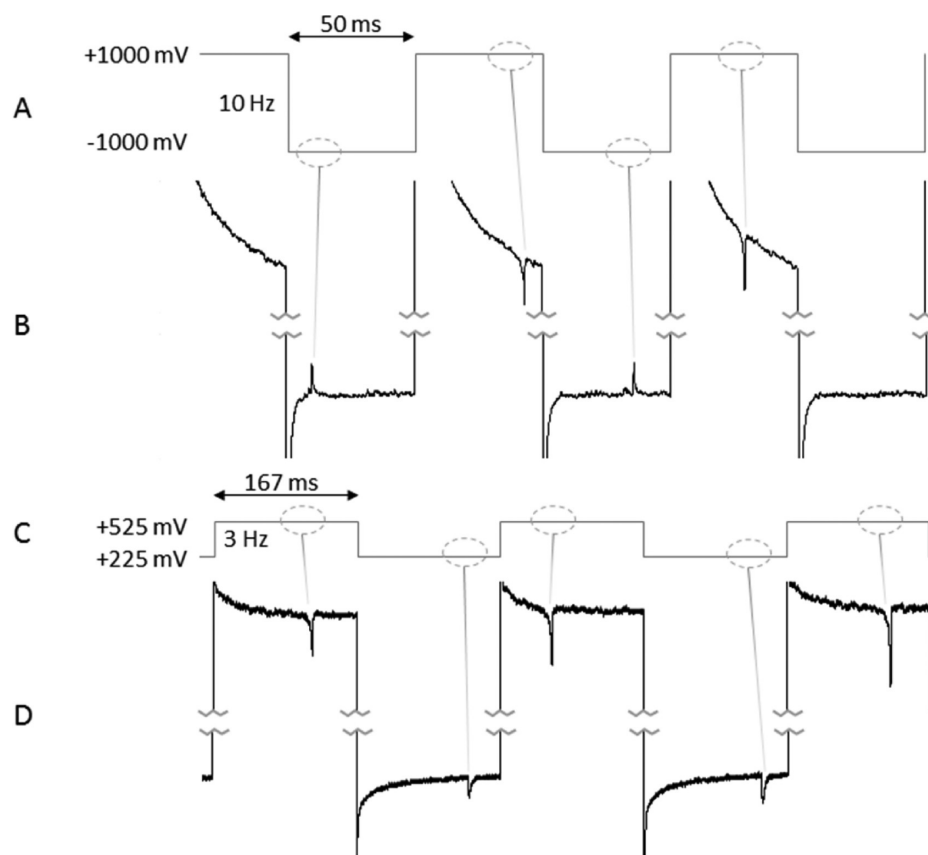


Figure 5. i - t traces showing a single nanoparticle passing back and forth through the nanopore orifice as the applied potential is reversed. (A) A 10 Hz voltage square wave between +1000 and -1000 mV results in resistive pulses in the i - t trace shown in (B). The i - t traces in (B) are clipped to show just the relevant 50 ms portions of the square wave where translocations occur. (C) A 3 Hz square wave between only +525 and +225 mV also results in a single nanoparticle passing back and forth through the pore orifice. Both solutions contained 8 nm Au nanoparticles ($\zeta = -51$ mV) in 1.0 M NaCl PBS pH 7.4 plus 0.1% Triton X-100. Particle concentration in (B) equals 50 nM, and in (D) equals 320 nM.

particle capture and release if pressure is applied additionally. This is illustrated in Figure 5C,D, where a square wave oscillating between +225 and +525 mV is sufficient to drive particles into and out of a pore as a constant negative pressure of ~ 0.05 atm is applied.

Controlling Nanoparticle Dynamics by Applied Pressure and Applied Potential. Either electrophoresis or applied pressure alone has typically been used as the single driving force for moving particles through a nanopore, as demonstrated in the previous section. Decreasing the particle translocation velocity by lowering voltage has limitations, however, because the signal-to-noise ratio is reduced dramatically as the voltage decreases. Here we report fine control of particle velocities by taking advantage of electroosmosis and by applying a constant pressure to shift the zero velocity point to a potential with acceptable signal-to-noise ratio (Figure 6). In this experiment, translocation velocities were assumed to be proportional to the inverse of the peak width at half-height, with positive values indicating translocations into the pipet. Negative pressures indicate fluid flow into the pipet; positive voltages are measured relative to the external solution (see Figure 1). At the outset of the experiment, the majority of 8 nm gold particles were outside of the pipet, except for a small number of particles that had been pulled into the pipet under pressure just prior. The pipet was then subjected to a constant negative pressure (-0.047 atm in Figure 6A and -0.35 atm in Figure 6B) and +500 mV. Both of these forces should act to drive negatively charged particles

into the pipet, and yet the particle translocation profiles clearly indicated that nanoparticles were expelled from the pipet. This is explained by the presence of a large electroosmotic flow that overpowers both the applied pressure and the electrophoretic forces acting on the particles under these conditions (Figure 1).¹⁰ For the experiments in Figure 6A, the contributions to the effective velocity made by applied pressure, electrophoresis, and electroosmosis are schematically illustrated in Figure 7. As the potential was ramped down to +100 mV over the course of 5 min, the EOF decreased at a faster rate than the EPF, and the driving forces acting on the particle were balanced at a characteristic transition voltage that was determined by the zeta potential of the particles. Particle velocities were markedly reduced at this transition. Of the 1890 translocations shown in Figure 6, 13 had peak widths greater than 20 ms and two were as large as ~ 200 ms. For the slowest translocations, the negation of all particle driving forces allowed us to see the effects of Brownian motion as the particle flickered in and around the sensing zone (blue trace inset in Figure 6A). This is in sharp contrast to the i - t traces recorded near the voltage limits where peak widths were ≤ 0.2 ms, representing an increase in particle velocity of 3 orders of magnitude. The limited number of translocations near 200–300 mV is a consequence of the diminishing particle rate of entry near the transition voltage, and of the small number of particles that initially is inside the pipet; the particles were eventually exhausted as the potential was decreased from 500 mV to the transition voltage. Below this voltage, particles were drawn into

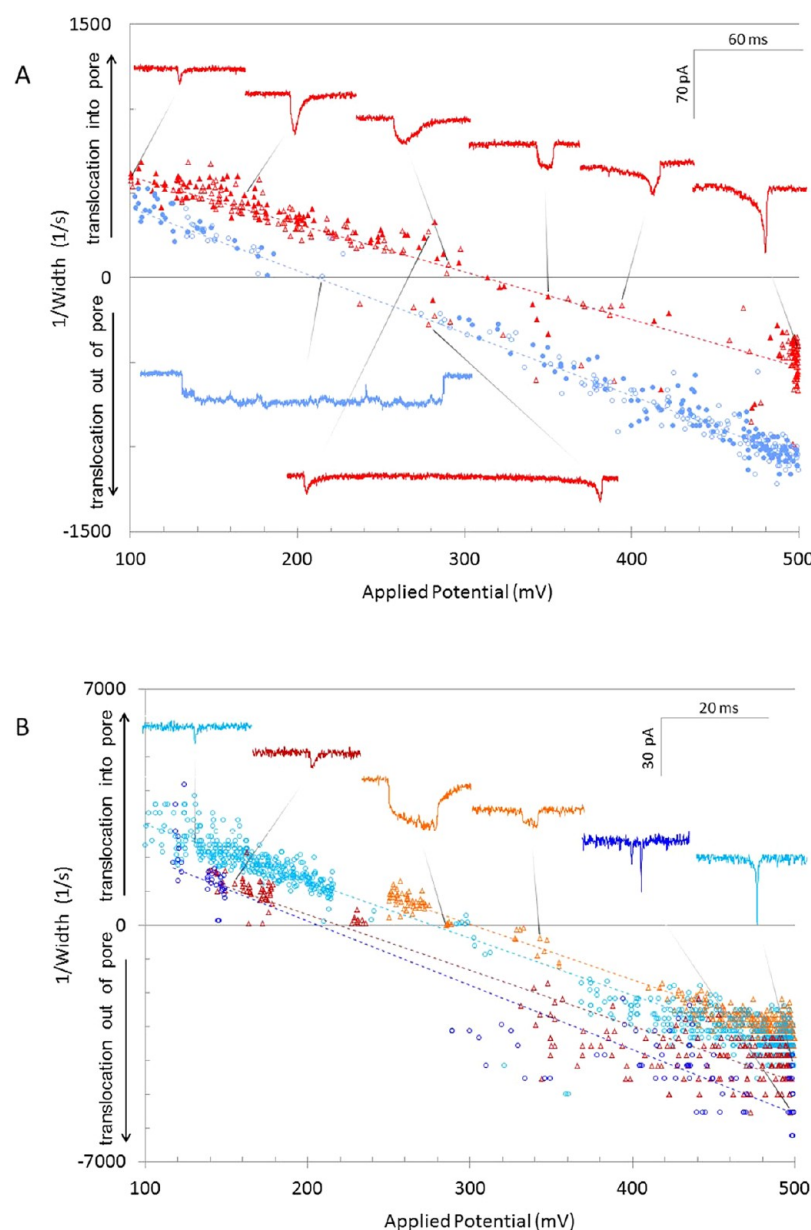


Figure 6. Nanoparticle translocation velocity vs applied voltage at a pressure of (A) -0.047 atm and (B) -0.35 atm. The solution conditions are for (A) 1.0 M NaCl (red $\triangle, \blacktriangle$, $\zeta = -51$ mV) and (blue \circ, \bullet , $\zeta = -15$ mV), and for (B) 0.2 M NaCl (orange \triangle , $\zeta = -51$ mV) and (turquoise \circ , $\zeta = -15$ mV); 0.1 M NaCl (dark red \triangle , $\zeta = -51$ mV) and (dark blue \circ , $\zeta = -15$ mV). All solutions were buffered at pH 7.4 with 7 mM Na_2HPO_4 , 21 mM KH_2PO_4 , and contained 0.1% Triton X-100. The filled and open symbols in (A) represent two consecutive sets of data collected under identical conditions. Dashed lines through data points represent linear least-squares fits. Representative $i-t$ traces for particular translocations at different voltages are shown.

the pipet from the external solution, as the combined EPF and applied pressure force became larger than the EOF.

Although there was considerable data scatter, the general trend was reproducible across two independent experiments carried out under identical conditions (Figure 6A, open and closed symbols). The experiments in Figure 6A were carried out with the same pipet (having a resistance of 110 M Ω at 1.0 M NaCl), and those in Figure 6B were all carried out with a different pipet (having a resistance of 125 M Ω at 1.0 M NaCl). Some of the data scatter at the highest and lowest applied potential is based on limitations in our ability to accurately measure peak width for the fastest moving particles (thus the digitization seen on the right of Figure 6B). Slow moving particles also involve scatter, presumably because additional

surface forces acting on the particles become significant under these conditions. The data scatter is particularly severe when the salt concentration is <0.2 M NaCl, mostly due to the relatively poor signal to noise. The experiments under low salt conditions (0.1 – 0.2 M NaCl) were done with a pore within 10 M Ω (measured at 1.0 M NaCl) of the threshold size in order to maximize the amplitude of the resistive pulses, particularly near 100 mV. The observation of several near zero velocity events that do not fall in line with the data trend likely indicates particles that have interacted strongly with the pore wall, because fluid flow was not fast enough to deter physisorption.

One additional source of apparent data scatter is cross contamination between experiments. For example, the $\zeta = -15$ mV data shown in Figure 6A was collected prior to the $\zeta = -51$

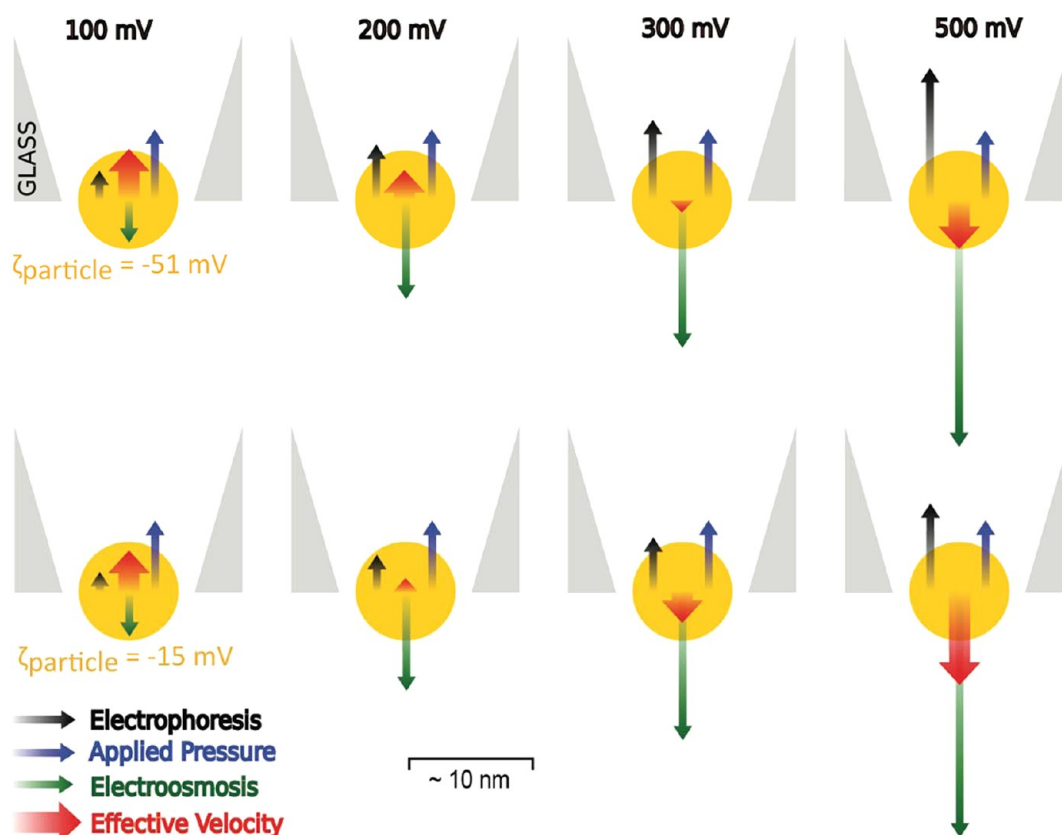


Figure 7. Schematic depicting control of nanoparticle velocity in conical nanopores. The voltage-dependent peak widths presented in Figure 6A result from the summed contributions of different forces acting on the charged nanoparticle. The applied pressure (-0.047 atm) remains constant throughout all measurements, but the *particle-dependent* electrophoretic and *particle-independent* electroosmotic forces change at different rates with varying voltage. As a result, the more highly charged particles ($\zeta = -51$ mV) obtain a minimum velocity at ~ 300 mV, while the less charged particles ($\zeta = -15$ mV) obtain a minimum velocity at ~ 200 mV.

mV data shown in the same figure, and despite efforts to thoroughly rinse the pipet between experiments, the red triangles falling in line with the $\zeta = -15$ mV data likely indicate the presence of residual $\zeta = -15$ mV particles. This assumption is supported by the fact that the signals show the opposite peak symmetry at the transition voltage of the $\zeta = -51$ mV particles. This is demonstrated by the lowest red inset in Figure 6A, which suggests that two particles, one with $\zeta = -15$ mV and one with $\zeta = -51$ mV, are crossing the pore in different directions at the same applied potential.

Factors Governing Particle Velocity. In resistive pulse sensing, particle velocities are governed by the relative strengths of the EPF, EOF, and applied pressure. While the EPF is a function of the charge of the particle, the EOF is only dependent upon the charge of the pore, and therefore the two forces increase with the applied voltage at different rates. Furthermore, these forces have different dependencies on pore geometry. Increasing the channel-like character of conical pores spreads the electric field over a larger sensing zone, which would be expected to reduce EPF. By contrast, increased pore channel length has been observed to increase the EOF.^{10,21} Although the geometry of the GNPs used in this study is conical, these GNPs have significant channel-like character due to the small half-cone angle ($\sim 2^\circ$), and this may be a key to achieving the delicate balance of the forces controlling particle dynamics.

Without applied pressure, the minimum particle velocity occurs at zero voltage, but with suitable pressure we are able to

shift the minimum velocity point to a voltage range that is convenient for measurements. Thus, for a particular pipet we applied a pressure necessary to place the transition voltage in this range; that is, the voltage at which particle velocities are minimized due to equivalence of the forces drawing particles into the pore (primarily the EPF and fluid flow caused by applied pressure) and those driving particles out of the pore (primarily the EOF). Firnkes et al. were able to balance the EPF and EOF by finding a pH at which the zeta potential of the pore and of the molecule studied were equal.¹⁰ However, simply eliminating the driving force does not allow for general control of particle dynamics. For the conical pores used in this study, the EOF appears to increase with voltage at a greater rate than the EPF, and we observed translocations in the opposite direction of electrophoresis under atmospheric conditions. Zhang et al. also demonstrated DNA translocating in the opposite direction of electrophoresis and attributed this to a large EOF.¹² In the experiments in Figure 6 we took advantage of the large change in EOF with respect to voltage, and were able to control the entire range of particle velocities from near zero to the limit of the electronic bandwidth filtering of the amplifier (10 kHz), in both the inward and outward direction and between $+100$ and $+500$ mV.

Finite Element Analysis (FEA) Simulations. Finite-element simulations using COMSOL Multiphysics were performed to provide a more quantitative description of the experimental results at each of the salt concentrations studied. We used a quasi-steady method which assumes that the fluid

and particle are in equilibrium.^{22–24} Based on the assumption that the sum of the hydrodynamic drag and electrokinetic forces (which account for pressure-driven flow and electro-osmosis flow) on the nanoparticle are zero, the velocity of the particle may be iteratively determined using the Newton–Raphson method to solve the following equations from an appropriate initial guess. Details of the simulation geometry and boundary conditions are provided in the Supporting Information.

A quasi-steady force balance is expressed as

$$\mathbf{F}_{\text{total}} = \mathbf{F}_H + \mathbf{F}_E = 0 \quad (1)$$

where \mathbf{F}_H and \mathbf{F}_E are hydrodynamic force and electrokinetic force exerted on the particle, respectively. These forces are given by eqs 2 and 3

$$\mathbf{F}_H = \int (\mathbf{T}_H \cdot \mathbf{n}) dS \quad (2)$$

$$\mathbf{F}_E = \int (\mathbf{T}_E \cdot \mathbf{n}) dS \quad (3)$$

where \mathbf{T}_H and \mathbf{T}_E are the hydrodynamic stress tensor and the Maxwell stress tensor, respectively, \mathbf{n} is the unit normal vector, and S represents the surface of the nanoparticle.

The Navier–Stokes equation describes the laminar flow of the incompressible fluid.

$$\rho \mathbf{u} \nabla \mathbf{u} = \frac{1}{\rho} (-\nabla p + \eta \nabla^2 \mathbf{u} - F(\sum_i z_i c_i) \nabla \Phi) \quad (4)$$

In eq 4, the body force component $-(F/\rho)(\sum_i z_i c_i) \nabla \Phi$ originates from the electroosmosis. \mathbf{u} and Φ are the local position-dependent fluid velocity and potential, c_i and z_i are concentration and charge of species i in solution, p is the pressure, and F is Faraday's constant. The solution density $\rho = 1000 \text{ kg/m}^3$ and the dynamic viscosity $\eta = 0.001 \text{ Pa}\cdot\text{s}$, respectively, correspond approximately to the aqueous solution. The particle velocity \mathbf{u} corresponds to the boundary velocity of the particle surface and surrounding fluid, eq 4.

The ion distribution and potential profile in the system are modeled by the Nernst–Planck–Poisson equations as below:

$$\mathbf{J}_i = -D_i \nabla c_i - \frac{Fz_i}{RT} D_i c_i \nabla \Phi + c_i \mathbf{u} \quad (5)$$

$$\nabla^2 \Phi = -\frac{F}{\epsilon} \sum_i z_i c_i \quad (6)$$

In eq 5, \mathbf{J}_i and D_i are the ion flux vector and diffusion coefficient of species i in solution, respectively. $D_{\text{Na}^+} = 1.33 \times 10^{-9} \text{ m}^2/\text{s}$ and $D_{\text{Cl}^-} = 2.03 \times 10^{-9} \text{ m}^2/\text{s}$. The absolute temperature $T = 298 \text{ K}$, and the gas constant $R = 8.314 \text{ J/K}$. ϵ is the dielectric constant of 78.

Figure 8 presents results of the FEA simulations corresponding to the experiments in Figure 6. Figure 8A shows velocity profiles and streamlines along the pore axis corresponding to the experimental conditions ($\zeta = -15 \text{ mV}$, 0.2 M NaCl and 0.35 atm external pressure) in Figure 6B (turquoise line). Using a half-cone angle of 1.87° , the general trends seen in the experiment were reproduced, with particles entering the pore at 100 mV , exiting the pore at 500 mV , and a crossover point occurring at $\sim 200 \text{ mV}$ (simulated) and $\sim 250 \text{ mV}$ (experimental). In Figure 8, B and C, simulation parameters were varied to reproduce the velocity trends seen in Figure 6, A and B, respectively, for the differently charged particles at varying

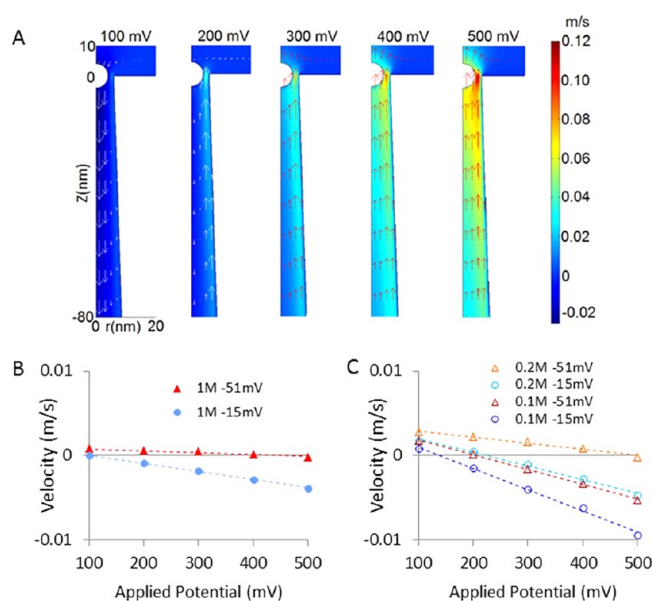


Figure 8. (A) Simulated velocity profile for a nanoparticle ($\zeta = -15 \text{ mV}$) in a 0.2 M NaCl solution, at 0.35 atm pressure and applied voltages between 100 and 500 mV corresponding to the turquoise lines in Figure 6B and panel C. (B,C) Plots of particle velocities corresponding to the data in Figure 6, A and B, respectively. The data point colors and symbols follow the same scheme used to plot experimental data in Figure 6. Parameters and other details of the finite-element simulation are presented in the Supporting Information file.

salt concentrations. A better quantitative match with experimental results is seen at the lower salt concentrations (Figure 8C). Specifically, the same velocity trends are seen as particle charge and the ionic strength of the solution are varied, with velocity reversal occurring in the 100 – 500 mV range. At higher salt concentration (Figure 8B) the agreement with the experimental measurements is weaker, but still qualitatively captures the trend in the experimental results. Given the approximations in the modeling parameters and the uncertainty in the nanopore geometry, the governing equations employed in the FEA simulations provide a very satisfactory description of the particle motion.

Effects of Salt Concentration and Particle Charge on Nanoparticle Dynamics. Experiments in 0.1 and 0.2 M NaCl solutions required a much larger applied pressure (-0.35 atm) than those in 1.0 M NaCl (-0.047 atm); the data are presented on a separate graph to accommodate a sufficiently wide range of particle velocities (Figure 6B). The need for higher pressure would be expected from the increased Debye lengths at lower salt concentrations, which generate larger EOFs along the pore surface. Since the EOF at the transition voltage is larger than the applied pressure, we can say that pressures greater than 0.3 atm are generated in 0.2 M NaCl at 300 mV , and in 0.1 M NaCl comparable pressures are generated at 200 mV . By contrast, Takamura et al. reported the fabrication of “extremely high pressure” electroosmotic pumps of 0.05 atm for $120 \text{ nm} \times 100 \mu\text{m}$ channels subjected to 40 V .²⁵

Examining the velocities of differently charged particles at a particular combination of salt concentration and applied voltage reveals the effect of particle charge. Under these conditions, the applied pressure and EOF are identical, and therefore the remaining electrophoretic force decreases the velocity of negative particles moving out of the pore and increases their

velocities as they move in. This explains why the velocity trend lines for the more highly charged ($\zeta = -51$ mV) particles were always above those for the less highly charged ($\zeta = -15$ mV) particles (Figure 6). It should be noted that the 0.1 M NaCl velocities fall below the 0.2 M NaCl due to an increased EOF and not because of charge effects.

Factors Affecting Resistive Pulse Peak Shape. It is well-known that the path of a particle through a conical nanopore determines the shape of a resistive pulse event. Inhomogeneity of the electric field within the sensing zone due to a stronger field near pore walls has been shown to cause as much as a 15% deviation in peak amplitude for particles that do not travel straight through the center of the pore (off-axial translocations).²⁶ Interaction of particles with pore walls can also lengthen translocation times, a factor that must be taken into account for analysis based upon peak widths.⁹ The ability to slow particle velocity to a degree achieved in our experiments allows a closer examination of the factors that affect translocation kinetics. This is illustrated by the insets in Figure 6A, which demonstrate clear peak shape differences during the course of translocations. In particular, we have observed the steep side of a typical asymmetric translocation exhibiting biphasic character to differing degrees (compare the rightmost inset translocation with both the second and the fifth translocation from right). These stages of resistance change may be explained by contributions from an inhomogeneous electric field, pore wall interactions, diffusion, and/or possibly a second EOF that arises from the double layer associated with the particle itself. An additional complicating factor could stem from the possibility that our pores were not entirely smooth throughout the sensing zone, although the observation of numerous “ideally shaped” translocations²⁷ argues against this possibility.

In summary, we have demonstrated that the dynamics of 8 nm nanoparticle translocations through micropipet GNPs can be controlled, and we have gathered important information about the interplay of electrophoretic, electroosmotic, and pressure forces by studying translocation velocity as a function of particle charge, salt concentration, and applied pressure. Detection and characterization of nanoparticles has a growing number of applications across different disciplines, from research and diagnostics to drug delivery, detection of nanoparticle waste released by industrial nanotechnology applications, and biosensing. Overcoming the problem of excessive particle velocities through appropriate choice of nanopores and observation parameters is an important step toward better understanding and applying these technologies. Controlling nanoparticle dynamics allows nanopore sensing to advance from mere *detection* of nanoparticles into the realm of nanoparticle *characterization* in a previously unattainable range.

METHODS

Materials. Spherical gold nanoparticles (diameter 8 nm $\pm 7\%$, SD, measured by TEM) conjugated with a carboxy methyl polymer were purchased from Nanopartz, Inc. (Loveland, CO). Zeta potentials were measured as -51 and -15 mV (Nanopartz) and as -52 and -22 mV (Particle Characterization Laboratories, Inc., Novato, CA) in deionized water, and as -38 and -12 mV in 0.1 M NaCl PBS pH 7.4 plus 0.1% Triton X-100 (Particle Characterization Laboratories, Inc.). Attempts to measure zeta potentials at higher salt concentrations yielded irreproducible values. The particles are denoted as -51 and -15 mV in the text even though ζ values are lower in salt

solutions. Other materials included borosilicate glass micropipets (o.d. 1.5 mm, i.d. 0.86 mm, length 10 cm, Sutter Instruments), hydrofluoric acid (48%), ammonium fluoride solution ($\sim 40\%$), ammonium fluoride etching mixture (AF 875-125, Sigma), pH 7.4 phosphate-buffered saline (PBS) 10X (Invitrogen), 3 M 12 μ m Lapping Film (Ted Pella), Triton-X100 (Amresco), 0.25 mm Ag wire (World Precision Instruments), household bleach (5% hypochlorite), and sodium bicarbonate (Costco). Solutions were filtered through Millex-GP, 0.22 μ m, polyethersulfone filters (Millipore).

Pipets. Pipets were pulled with a Model P-1000 Flaming/Brown micropipet puller (Sutter Instruments) to a ~ 1 μ m opening. Pulled pipet tips were then melted with a butane hand torch (flame tip positioned ~ 5 mm from the tip) for ~ 130 ms as the pipets rotate on a turntable at 3.5 cm/s. Sanding of the resulting terminal bulb was carried out by hand prior to microforge heating, which involved placing the pipet tip within a Ω -shaped platinum–iridium alloy filament (5 mm \times 5 mm) heating element made from a 5 mm wide platinum/iridium strip for ~ 400 ms. Pipet tips were initially imaged using an inverted Olympus IX50 microscope, and then a few were selected for SEM imaging with an FEI Helios Nanolab 600 Dual-Beam FIB.

Glass Nanopore Fabrication. Borosilicate glass micropipets were heated at 600 $^{\circ}$ C for 12 h and then immediately sealed at both ends. After being pulled to an ~ 1 μ m opening, they were kept under a stream of dry nitrogen until the sharp tip was melted. The terminal bulb inclosing a conical cavity was then sanded to a flattened tip using fine sandpaper followed by microforge heating. Just prior to etching, the other end of the pipet was opened, fire polished, and backfilled with 1.0 M NaCl. Ag/AgCl electrodes were prepared by immersing an Ag wire in bleach for ~ 15 min prior to experiments and were placed inside multiple pipets connected in parallel as well as the etchant solution (a 1:2 dilution of 48% hydrofluoric acid in a $\sim 40\%$ ammonium fluoride solution). Pore formation was indicated by a jump in current measured using a Princeton Applied Research 2273 PARSTAT potentiostat operating in current versus time mode with 250 mV applied potential. Pipet tips were immediately dipped into 3 M KOH for 10 s and transferred to a 1.0 M NaCl solution for current measurements. Pores having resistances between 100 and 200 M Ω were routinely made in this way, etched to larger sizes as needed by dipping briefly (15 s) into a 1:20 dilution of ammonium fluoride etching mixture (AF 875-125), and repeating the etching process until threshold translocations no longer occurred.

Resistive Pore Sensing Measurements and Data Analysis. Pipets were placed into a BNC style electrode holder that allowed for application of pressure within the pipet (Warner Instruments), and current were measurements made using a HEKA EPC-10 amplifier at a cutoff frequency of 3 kHz applied with a three-pole Bessel low-pass filter. PatchMaster data acquisition software was used to initially analyze and export current–time traces. A custom VBA Excel program was used to determine translocation peak parameters such as peak position, height, and width at half-height as a function of applied voltage. Each peak was inspected manually to ensure accurate measurements; in general, resistive pulses having a signal-to-noise ratio of less than 7:1 and/or a base width of less than 1 ms were excluded.

Finite-Element Simulations. The finite-element simulations were performed using COMSOL Multiphysics 3.5 (Comsol, Inc.) on a high-performance desktop PC.

■ ASSOCIATED CONTENT

● Supporting Information

Pressure-controlled reversal of particle translocation, calculation of Au nanoparticle charge density, and details of the finite-element simulations used to compute nanoparticle velocities. This material is available free of charge via the Internet at <http://pubs.acs.org>.

■ AUTHOR INFORMATION

Corresponding Author

*Tel.: 253-922-2600. E-mail: tmega@revalesio.com.

Notes

The authors declare the following competing financial interest(s): Sean German and Tony Mega are employees of Revalesio Corporation.

■ ACKNOWLEDGMENTS

The authors acknowledge S. Krämer for SEM imaging at the Materials Department of the University of California at Santa Barbara and A. Kalmes of Revalesio Corp. for manuscript editing. L.L. acknowledges financial support provided by predoctoral fellowship from University of Utah Nanotechnology Training Program.

■ REFERENCES

- (1) Domingos, R.; Baalousha, M.; Ju-Nam, Y.; Reid, M.; Tufenkji, N.; Lead, J.; Leppard, G.; Wilkinson, K. *Environ. Sci. Technol.* **2009**, *43*, 7277–7284.
- (2) DeBlois, R. W.; Bean, C. P.; Wesley, R. K. A. *J. Colloid Interface Sci.* **1977**, *61*, 323–335.
- (3) Lan, W.-J.; Holden, D. A.; Zhang, B.; White, H. S. *Anal. Chem.* **2011**, *83*, 3840–3847.
- (4) Wu, H.-C.; Astier, Y.; Maglia, G.; Mikhailova, E.; Bayley, H. *J. Am. Chem. Soc.* **2007**, *129*, 16142–16148.
- (5) Wanunu, M.; Sutin, J.; Ben McNally; Chow, A.; Meller, A. *Biophys. J.* **2008**, *95*, 4716–4725.
- (6) Wanunu, M.; Dadosh, T.; Ray, V.; Jin, J.; McReynolds, L.; Drndić, M. *Nature Nanotechnol.* **2010**, *5*, 807–814.
- (7) Fologea, D.; Uplinger, J.; Thomas, B.; McNabb, D. S.; Li, J. *Nano Lett.* **2005**, *5*, 1734–1737.
- (8) Berge, L. I.; Feder, J.; Jøssang, T. *Rev. Sci. Instrum.* **1989**, *60*, 2756–2763.
- (9) Gershow, M.; Golovchenko, J. A. *Nature Nanotechnol.* **2007**, *2*, 775–779.
- (10) Firnkes, M.; Pedone, D.; Knezevic, J.; Döblinger, M.; Rant, U. *Nano Lett.* **2010**, *10*, 2162–2167.
- (11) Ito, T.; Sun, L.; Crooks, R. M. *Anal. Chem.* **2003**, *75*, 2399–2406.
- (12) Zhang, B.; Wood, M.; Lee, H. *Anal. Chem.* **2009**, *81*, 5541–5548.
- (13) Vogel, R.; Anderson, W.; Eldridge, J.; Glossop, B.; Willmott, G. *Anal. Chem.* **2012**, *84*, 3125–3131.
- (14) Venkatesan, B. M.; Bashir, R. *Nature Nanotechnol.* **2011**, *6*, 615–624.
- (15) Howorka, S.; Siwy, Z. *Chem. Soc. Rev.* **2009**, *38*, 2360–2384.
- (16) Gao, C.; Ding, S.; Tan, Q.; Gu, L.-Q. *Anal. Chem.* **2009**, *81*, 80–86.
- (17) Li, G.-X.; Zhang, Z.-X.; Lin, X.-Q. *Chin. J. Anal. Chem.* **2010**, *38*, 1698–1702.
- (18) White, H. S.; Bund, A. *Langmuir* **2008**, *24*, 2212–2218.
- (19) Vercoutere, W.; Winters-Hilt, S.; Olsen, H.; Deamer, D.; Haussler, D.; Akeson, M. *Nat. Biotechnol.* **2001**, *19*, 248–252.
- (20) Lan, W.-J.; White, H. S. *ACS Nano* **2012**, *6*, 1757–1765.
- (21) Yusko, E. C.; An, R.; Mayer, M. *ACS Nano* **2010**, *4*, 477–487.
- (22) Ye, C.; Sinton, D.; Erickson, D.; Li, D. *Langmuir* **2002**, *18*, 9095–9101.
- (23) Yalcin, S. E.; Lee, S. Y.; Joo, S. W.; Baysal, O.; Qian, S. J. *Phys. Chem. B* **2010**, *114*, 4082–4093.
- (24) Jubery, T. Z.; Prabhu, A. S.; Kim, M. J.; Dutta, P. *Electrophoresis* **2012**, *33*, 325–333.
- (25) Takamura, Y.; Onoda, H.; Inokuchi, H.; Adachi, S.; Oki, A.; Horiike, Y. *Electrophoresis* **2003**, *24*, 185–192.
- (26) Kozak, D.; Anderson, W.; Vogel, R.; Trau, M. *Nano Today* **2011**, *6*, 531–545.
- (27) Lan, W. J.; Holden, D. A.; Liu, J.; White, H. S. *J. Phys. Chem. C* **2011**, *115*, 18445–18452.